Journal of Inorganic Biochemistry 249 (2023) 112397

Contents lists available at ScienceDirect

Journal of Inorganic Biochemistry

journal homepage: www.elsevier.com/locate/jinorgbio

Mitochondria-targeted cyclometalated iridium (III) complexes: Dual induction of A549 cells apoptosis and autophagy

Lanmei Chen [a,b,c,1], Hong Tang [a,b,c,1], Weigang Chen [a], Jie Wang [a], Shenting Zhang [a,b,c], Jie Gao [a,b], Yu Chen [a], Xufeng Zhu [b,c,*], Zunnan Huang [a,b,c,*], Jincan Chen [a,b,c,*]

[a] Key Laboratory of Computer-Aided Drug Design of Dongguan City, Guangdong Key Laboratory for Research and Development of Natural Drugs, School of Pharmacy, Guangdong Medical University, Dongguan, Guangdong 523808, PR China

[b] The Marine Biomedical Research Institute, Guangdong Medical University, Zhanjiang, Guangdong 524023, PR China

[c] The Marine Biomedical Research Institute of Guangdong Zhanjiang, Zhanjiang, Guangdong 524023, PR China

A R T I C L E I N F O

Keywords:
Iridium complexes
Mitochondria
A549 cells
Apoptosis
Autophagy

A B S T R A C T

In this study, we synthesized 4 cyclometalated iridium complexes using N-(1,10-phenanthrolin-5-yl)picolinamide (PPA) as the main ligand, denoted as $[Ir(ppy)_2PPA]PF_6$ (ppy = 2-phenylpyridine, Ir1), $[Ir(bzq)_2PPA]PF_6$ (bzq = benzo[*h*]quinoline, Ir2), $[Ir(dfppy)_2PPA]PF_6$ (dfppy = 2-(3,5-difluorophenyl)pyridine, Ir3), and $[Ir(thpy)_2PPA]PF_6$ (thpy = 2-(thiophene-2-yl)pyridine, Ir4). Compared to cisplatin and oxaliplatin, all four complexes exhibited significant anti-tumor activity. Among them, Ir2 demonstrated higher cytotoxicity against A549 cells, with an IC_{50} value of 1.6 ± 0.2 μM. The experimental results indicated that Ir2 primarily localized in the mitochondria, inducing a large amount of reactive oxygen species (ROS) generation, that decreased in mitochondrial membrane potential (MMP), reduced ATP production, and further impaired mitochondrial function, leading to cytochrome *c* release. Additionally, Ir2 caused cell cycle arrest at the S phase and induced apoptosis through the AKT-mediated signaling pathway. Further investigations revealed that Ir2 could simultaneously induce both apoptosis and autophagy in A549 cells, with the latter acting as a non-protective mechanism that promoted cell death. More importantly, Ir2 exhibited low toxicity to both normal LO2 cells in vitro and zebrafish embryos in vivo. Consequently, these newly developed Ir(III) complexes show great potential in the development of novel and low-toxicity anticancer agents.

1. Introduction

Cancer is recognized as one of the leading causes of death worldwide [1]. Among these cancers, lung cancer accounts for 11.6% of the total diagnosed cases of cancer globally [2]. Lung cancer is classified into small-cell lung cancer (SCLC) and non-small-cell lung cancer (NSCLC), with the latter comprising nearly 85% of cases [3]. According to relevant literature, the number of cancer-related deaths caused by lung cancer exceeds the sum of breast cancer, prostate cancer, and colorectal cancer [4]. The treatment of NSCLC faces significant challenges, as many late-stage lung cancer patients are unable to tolerate the side effects of chemotherapy [5]. Therefore, there is an urgent need to explore a treatment approach that is both low in side effects and highly efficient.

Some metal-based complexes, such as iridium, ruthenium, rhenium, gold, and platinum, exhibit certain roles in cancer treatment. These metal complexes target the cell nucleus, mitochondria, and endoplasmic

Abbreviations: PPA, N-(1,10-phenanthrolin-5-yl)picolinamide; PBS, phosphate buffered saline; ppy, 2-phenylpyridine; bzq, benzo[*h*]quinoline; dfppy, 2-(3,5-difluorophenyl)pyridine; thpy, 2-(thiophen-2-yl)pyridine; MTT, 3-(4,5-dimethylthiazol-2-yl)-2,5-diphenyltetrazolium bromide; ICP-MS, Inductively Coupled Plasma Mass Spectrometry; ROS, reactive oxygen species; ESI-MS, electrospray ionization mass spectrometry; FBS, fetal bovine serum; MMP, mitochondrial membrane potential; JC-1, 5,5′6,6′-tetrachloro-1,1′,3,3′-tetraethylimidacarbocyanine iodide; DCFH-DA, 2,7-dichlorodi-hydroflfluorescein diacetate; DMEM, dulbecco's modified eagle medium; ATP, Adenosine Triphosphate; SCLC, small-cell lung cancer; NSCLC, non-small-cell lung cancer; PA, Pyridinic acid; NO, nitric oxide; DMSO, dimethyl sulphoxide; HOBT, hydroxybenzotriazole; DIEA, N, N-diisopropylethylamine; EDCI, 1-Ethyl-3-(3-dimethylaminopropyl)carbodiimide; LTR, Lyso Tracker Red; MTR, Mito Tracker Red; CDKs, cyclin-dependent kinases; MDC, Monodansylcadaverine; AO, Anthracene Orange; AVOAs, acidic vacuolar organelles; TEM, transmission electron microscopy; PS, Phosphatidylserine; UV–vis, ultraviolet visible; SDS-PAGE, sodium dodecyl sulfate-polyacrylamide gel electrophoresis..

* Corresponding authors.
E-mail addresses: xufeng910730@126.com (X. Zhu), zn_huang@gdmu.edu.cn (Z. Huang), chenjc@gdmu.edu.cn (J. Chen).

[1] These authors contributed equally to this work.

https://doi.org/10.1016/j.jinorgbio.2023.112397
Received 11 August 2023; Received in revised form 1 October 2023; Accepted 6 October 2023
Available online 14 October 2023
0162-0134/

reticulum [6–10]. As is well known, the exceptional properties of molecules originate from their unique structural characteristics [11]. Compared to organic compounds, metal-based complexes possess greater flexibility in structure, making it easier to introduce other molecular functional groups on ligands for specific structural modifications in different substrate binding environments. Additionally, metal-based complexes are relatively stable, allowing for efficient drug effects within the body [12]. Compared to platinum-based complexes, iridium complexes exhibit higher tumor cell selectivity with lesser toxicity to normal cells [13,14]. In recent years, cyclometalated iridium(III) complexes have aroused significant interest among researchers due to their excellent photophysical, photochemical properties, and antitumor mechanisms [15–19].

Previously, our group synthesized a series of metal-based ruthenium and iridium complexes, which primarily targeted the cell mitochondria [19–21]. Mitochondria, as the energy supplier of cells, are double-membraned organelles in the cytoplasm of eukaryotic cells, serving as the main oxygen-consuming powerhouses [22]. Mitochondria play crucial roles in various physiological processes, apart from providing energy to cells. They are involved in processes such as cell differentiation, cell signaling, and cell apoptosis, and possess the ability to regulate cell growth and the cell cycle. Damage or defects in mitochondria can lead to diseases, such as neurodegenerative disorders, metabolic diseases, and cancer [23]. Therefore, mitochondria are considered potential targets for many chemotherapy drugs.

Pyridinic acid (PA) is a natural catabolic product of L-tryptophan metabolism synthesized by pyridoxine decarboxylase from 2-amino-3-carboxy aldehyde [24]. PA exhibits various biological activities, such as activating murine macrophages, inducing nitric oxide synthase and nitric oxide (NO) production, inducing interleukin-8 (IL-8) production, and demonstrating anticancer effects [25,26]. PA or its derivatives can directly coordinate with metal centers, and such complexes possess certain antitumor, antimicrobial, or topoisomerase inhibitory activities. For instance, Liu et al. linked PA derivatives with metal iridium, resulting in complexes with significant antitumor activity, exhibiting a 5-fold increase in IC_{50} value against A549 cells compared to cisplatin [27]. Chew-Hee Ng et al. designed and synthesized metal-based zinc-PA complexes with topoisomerase I inhibitory activity [28]. Amanda Lee E. Manicum et al. connected pyridinic acid and its fluorinated derivatives with metal rhenium, synthesizing complexes that demonstrated promising cytotoxicity against HeLa and A549 cells [29].

Based on this, in this study, we modified PA and obtained N-(1,10-phenanthrolin-5-yl)picolinamide (PPA) through condensation reaction with 5-amino-1,10-phenanthroline, and used it as the main ligand to design and synthesize four cyclometalated iridium complexes, $[Ir(ppy)_2PPA]PF_6$ (Ir1), $[Ir(bzq)_2PPA]PF_6$ (Ir2), $[Ir(dfppy)_2PPA]PF_6$ (Ir3), and $[Ir(thpy)_2PPA]PF_6$ (Ir4), and their structures were characterized. To elucidate their antitumor mechanism, we investigated the cellular uptake, subcellular localization, impact on mitochondria and reactive oxygen species, anticancer activities, and in vivo safety of these iridium complexes. The results demonstrated that all synthesized iridium complexes Ir1-Ir4 exhibited significant in vitro activity against tested tumor cell lines. ICP-MS and laser scanning confocal microscope analysis revealed that all 4 complexes were localized in the mitochondria. Moreover, complex Ir2 induced mitochondrial dysfunction, cytochrome *c* release, cell cycle arrest at the S phase, and further triggered apoptosis and autophagy. Importantly, the 4 complexes showed certain safe concentrations in vivo, as the zebrafish embryos exhibited a hatching rate and survival rate over 80% at 96 h when the concentrations of Ir1-Ir4 were below this threshold.

Table 1
IC_{50} values of tested compounds towards different cell lines.

Complex	IC_{50}[a] (μM)					
	A549	HeLa	HepG2	MCF-7	LO2	SI[b]
PPA	60.6 ± 0.2	71.1 ± 0.5	68.2 ± 0.7	75.5 ± 0.3	80.5 ± 0.9	1.33
Ir1	3.3 ± 0.5	3.6 ± 0.4	4.9 ± 0.6	3.7 ± 0.6	13.7 ± 0.9	4.15
Ir2	1.6 ± 0.2	1.8 ± 0.3	3.4 ± 0.6	4.1 ± 0.4	12.2 ± 0.6	7.63
Ir3	5.2 ± 0.2	6.3 ± 0.4	7.8 ± 0.2	5.9 ± 0.7	16.9 ± 0.7	3.25
Ir4	4.3 ± 0.4	5.1 ± 0.2	4.7 ± 0.5	6.6 ± 0.6	16.4 ± 0.9	3.81
Cisplatin	18.6 ± 1.6	21.8 ± 2.1	20.4 ± 1.5	13.5 ± 1.1	17.8 ± 1.2	0.96
Oxaliplatin	13.5 ± 0.9	11.8 ± 1.2	17.9 ± 1.3	13.1 ± 1.1	15.7 ± 0.9	1.16

[a] IC_{50} values are drug concentrations necessary for 50% inhibition of cell viability. Data are presented as mean ± standard deviation and cell viability was assessed after 48 h incubation.
[b] SI (selectivity index) = IC_{50} (LO2)/IC_{50} (A549).

2. Results and discussion

2.1. Synthesis and characterization

The synthetic routes for Ir1-Ir4 are depicted in Scheme S1 (Supporting information text). Starting with 2-pyridinic acid and 1,10-phenanthrolin-5-amine as raw materials, hydroxybenzotriazole (HOBT), N, N-diisopropylethylenediamine (DIEA), and 1-ethyl-(3-dimethylaminopropyl)carbodiimide hydrochloride (EDCI) were added. The reaction was refluxed at 298 K for 24 h, resulting in the formation of the main ligand PPA. The iridium complexes precursor, $Ir(C^N)_2Cl_2$, was obtained by reacting hydrated iridium trichloride, $IrCl_3 \cdot 3H_2O$, with the corresponding C^N ligands (ppy, dfppy, bzq, and thpy). The iridium complexes Ir1-Ir4 were directly synthesized by connecting the iridium precursors with the main ligand according to the reported literature methods [30]. The chemical structures of iridium complexes Ir1-Ir4 are shown in Fig. 1A.

The main ligand, PPA, and complexes Ir1-Ir4 were characterized by elemental analysis, ESI-MS (Fig. S1-S4), and ^1H NMR (Fig. S5-S9). In the ^1H NMR spectrum of PPA, a distinct peak at 11.12 ppm corresponding to the amide bond proton (N—H, N15) was observed (Fig. S5), indicating the successful condensation of the amide bond. In the ESI-MS spectra of Ir1-Ir4, ion peaks at 801.12 (Ir1), 849.11 (Ir2), 871.20 (Ir3), and 811.12 (Ir4) $[M\text{-}PF_6]^+$ were detected, matching the theoretical values, confirming the successful synthesis of the corresponding iridium complexes (Fig. S1-S4). Furthermore, upon coordination with iridium metal ions, the ^1H NMR signals of the CH protons (Ar—H, C7, C8) adjacent to the N atoms in the main ligand PPA were affected by changes in the electronic cloud density upon ligand coordination with the metal atom. During the formation of Ir1-Ir4, the ^1H NMR signals of PPA's CH protons (Ar—H, C7, C8) experienced a noticeable shift from 9.16 ppm and 9.09 ppm towards higher magnetic fields. As a result, the corresponding signals around 9.16 ppm and 9.09 ppm were not observed in the ^1H NMR spectra of Ir1-Ir4. Additionally, after coordination with iridium metal ions, the other proton signals in the PPA moiety did not show significant changes. For instance, the signal of the CH proton (Ar—H, C20) adjacent to the N atom remained nearly the same in the ^1H NMR spectra of Ir1-Ir4, located around 8.84 ppm. Moreover, in the ^1H NMR spectra of Ir1-Ir4, clear signals at 11.46 ppm (Ir1), 11.47 ppm (Ir2), 11.48 ppm (Ir3), and 11.47 ppm (Ir4) corresponding to the amide bond protons were observed (Fig. S6-S9), further confirming the successful coordination of the main ligand.

Fig. 1B displays the UV–Vis absorption spectra of Ir1-Ir4 in CH_3CN solution at 298 K. Three distinct absorption bands are observed within the range of 200–600 nm. Ir1-Ir4 exhibit prominent absorptions at 265 nm, 261 nm, 250 nm, and 275 nm, while the absorption peaks at 331 nm and 419 nm are relatively broad [31].

The absorption spectra in the CH_2Cl_2 solution and PBS buffer (pH = 7.4) also exhibited similar results (Fig. 1C, D). Furthermore, in the

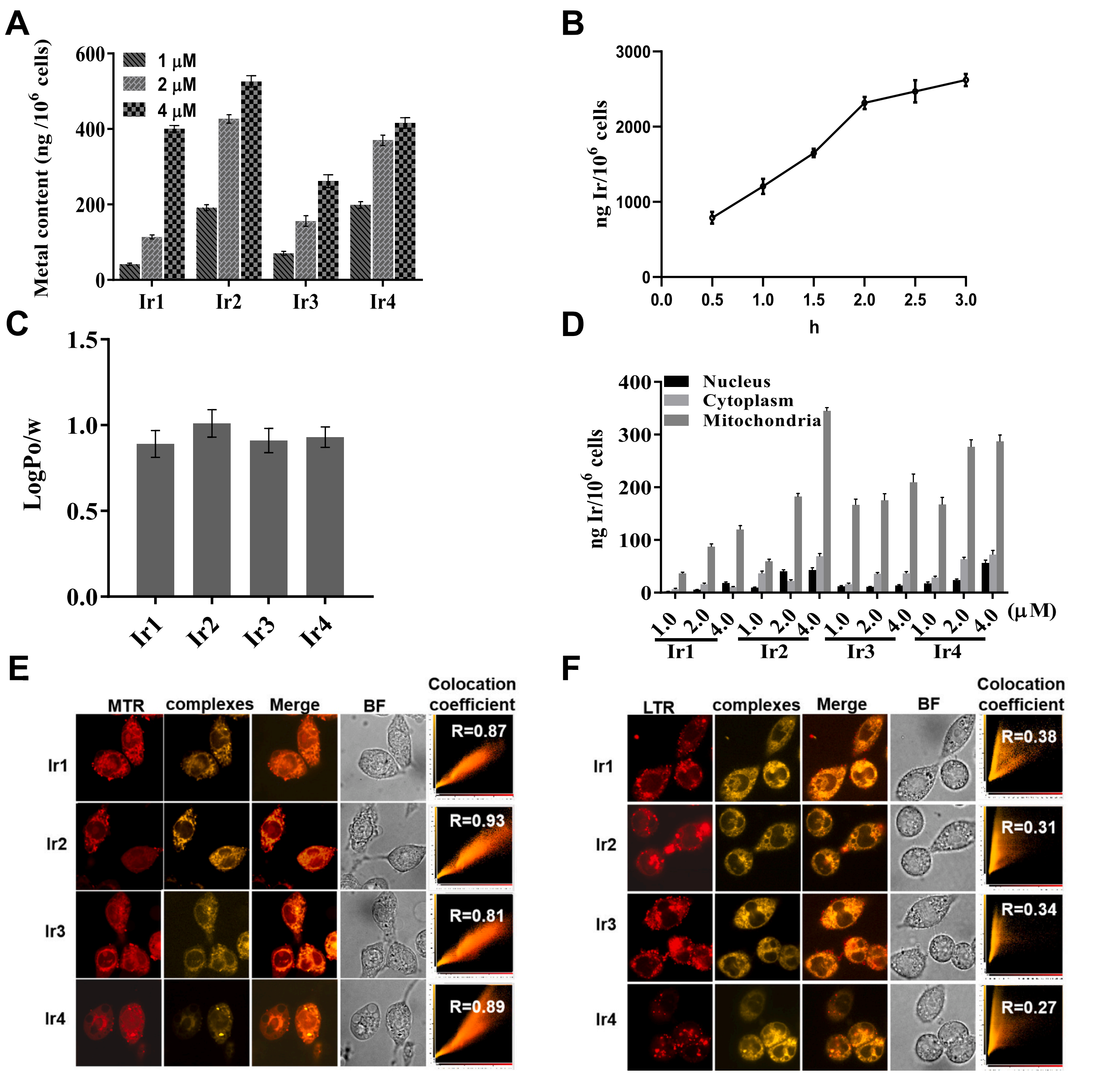

Fig. 2. Cellular uptake and distribution of Ir1-Ir4 in A549 cells. (A) Cellular Ir contents were determined in A549 cells after 24 h incubated with 1, 2, and 4 μM Ir1-Ir4, respectively. (B) Cellular Ir contents were determined in A549 cells incubated with 2 μM Ir2 in 3 h. (C) Log$P_{O/W}$ values of Ir1-Ir4. (D) Subcellular distribution of Ir content in A549 cell after incubated with 1, 2, 4 μM Ir1-Ir4 for 24 h CLSM images of A549 cells co-labeled with Ir complexes (2 μM, 3 h), and (E) Lyso Tracker Red (LTR; 50 nM, 30 min). $\lambda_{ex} = 561$ nm, $\lambda_{em} = 617 \pm 36$ nm (LTR), (F) Mito Tracker Red (MTR; 150 nM, 30 min). $\lambda_{ex} = 561$ nm, $\lambda_{em} = 617 \pm 36$ nm (MTR) and $\lambda_{ex} = 405$ nm, $\lambda_{em} = 560 \pm 40$ nm (Ir complexes); All images share the same scale bar: 10 μm. (For interpretation of the references to colour in this figure legend, the reader is referred to the web version of this article.)

fluorescence spectroscopic measurements, complexes Ir1-Ir4 showed distinct emission peaks upon excitation at 405 nm, while emission peaks were negligible when excited at 488 nm (Fig. S10), consistent with the confocal microscopy analysis results (Fig. S11). As shown in Fig. 1E, F, G, the emission wavelength of Ir3 under 405 nm excitation was 520 ± 20 nm, while both Ir1 and Ir2 exhibited red-shifted emission peaks at 560 ± 20 nm. Notably, compared to Ir1-Ir3, complex Ir4 demonstrated the largest redshift in emission wavelength, located at 600 ± 20 nm. Finally, we assessed the stability of complexes Ir1-Ir4. As shown in Fig. S12, after incubation in PBS buffer for 72 h, the UV–Vis spectra of the complexes remained almost unchanged, indicating good stability of these complexes in PBS buffer.

2.2. *In vitro antiproliferative activity*

To evaluate the in vitro cytotoxicity of the synthesized iridium complexes, we tested them against four tumor cell lines (A549, Hela, HepG2, and MCF-7) and one normal cell line (LO2). Cisplatin and oxaliplatin were used as control compounds. The MTT assay was employed for screening, and the results are shown in Table 1. All iridium complexes exhibited significant toxicity against the selected tumor cell lines, with the cytotoxicity ranking as follows: Ir2 > Ir1 > Ir4 > Ir3. Particularly, Ir2 demonstrated the highest cytotoxicity against A549 cells, with an IC_{50} value of 1.6 ± 0.2 μM, which was 11-fold higher than that of cisplatin and 8-fold higher than that of oxaliplatin. Notably, the

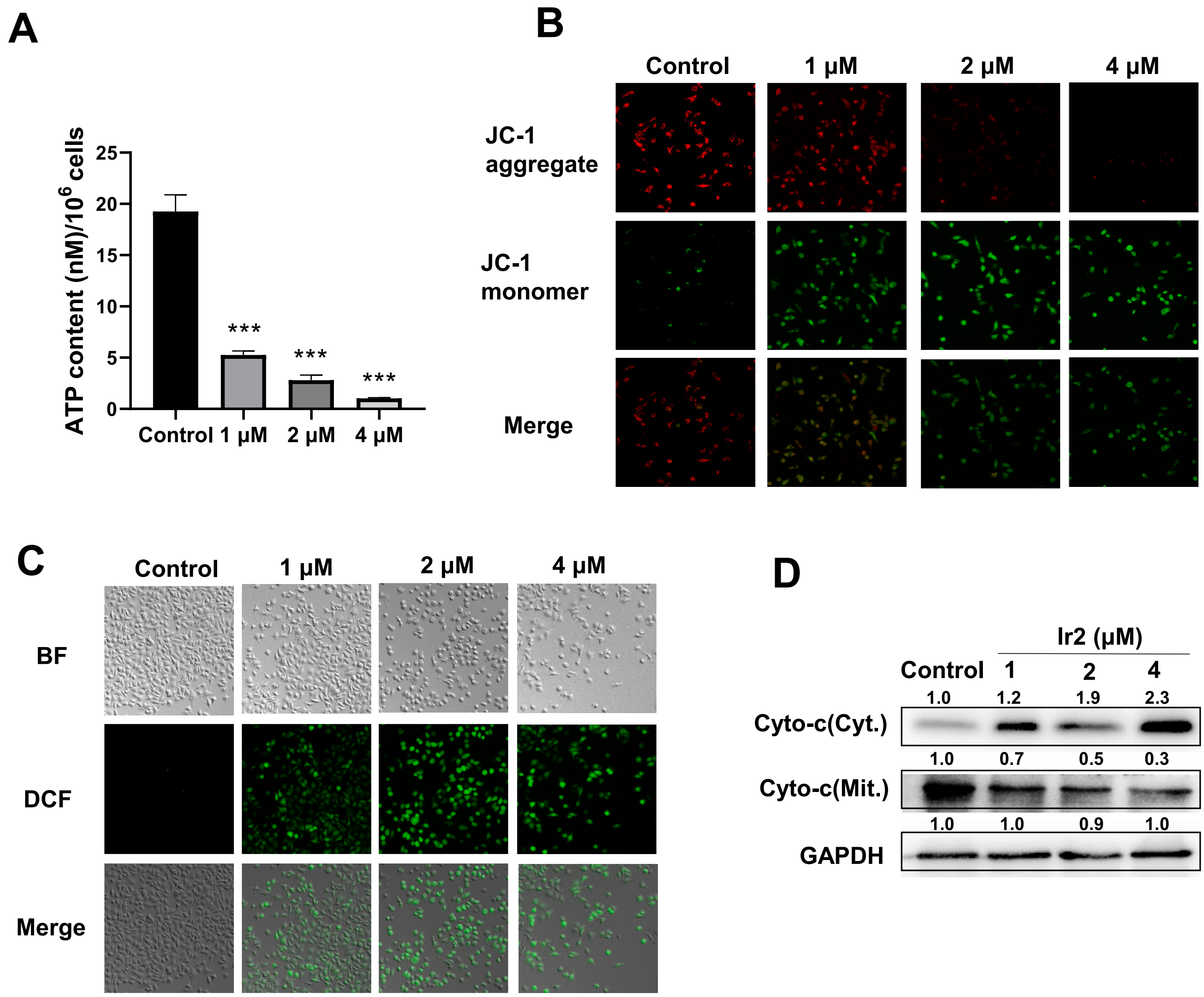

Fig. 3. (A) The ATP levels in A549 cell after incubation with 1, 2, 4 μM Ir2 for 12 h. CLSM images of (B) JC-1 stained and (C) ROS stained A549 cells after treatment with Ir2 (1,2,4 μM) for 12 h. scale bar: 100 μm. (D) Western blotting analysis of Cyto-*c* (Cyt.)and Cyto-*c* (Mit.) protein in A549 cells treated with Ir2 (1,2,4 μM) for 12 h. GAPDH was used as an internal control. DCF, $\lambda_{ex} = 488$ nm, $\lambda_{em} = 525 \pm 25$ nm; JC-1 aggregate, $\lambda_{ex} = 585$ nm, $\lambda_{em} = 595 \pm 20$ nm; JC-1 monomer, $\lambda_{ex} = 488$ nm, $\lambda_{em} = 525 \pm 25$ nm. Scale bar: 100 μm. The data are presented as mean ± standard deviation (SD) with ***$P < 0.001$.

antiproliferative activity of the 4 complexes against the normal cell line LO2 was lower compared to the other tumor cells, with a selectivity index of 4.15, 7.63, 3.25, and 3.81, all higher than those of cisplatin (0.96) and oxaliplatin (1.16), indicating Ir1-Ir4 have certain selectivity towards human cancer cells.

2.3. Cellular uptake and subcellular localization

The cellular uptake level of complexes is correlated with their cytotoxicity, generally, the more uptake, the stronger the cytotoxicity [31]. To elucidate the relationship between cellular uptake and cytotoxicity, we employed ICP-MS to measure the intracellular iridium content. As shown in Fig. 2A, after incubating the iridium complexes with A549 cells for 24 h, the intracellular iridium content increased in a concentration-dependent manner. Among them, Ir2 exhibited the highest uptake among the four complexes, with a content of 522 ± 12 ng of metal iridium per 10^6 cells at a concentration of 4 μM, followed by Ir1 and Ir4 with 415 ± 12 ng, while Ir3 complex showed the least cellular uptake, with metal iridium content of 263 ± 14 ng. These are consistent with the results of cellular cytotoxicity in vitro. Furthermore, we observed that the intracellular iridium content of Ir2 increased in a time-dependent manner within 3 h of incubation with A549 cells (Fig. 2B). Similar results were observed by using confocal microscopy (Fig. S13), where the yellow fluorescence intensity of Ir2 in cells gradually increased with longer incubation time, indicating an accumulation of iridium within the cells.

The lipophilic (log *P* value) is used to evaluate pharmacokinetic parameters related to drug action, such as lipophilicity, cellular uptake, metabolism, and bioavailability [32]. In order to assess the lipophilicity of the iridium complexes, we determined the water-octanol partition coefficient (*P*) using a conventional shake-flask technique. Log *P* values ≤ -4 indicate poor lipid bilayer permeability, while values ≥ 4 indicate poor water solubility [33]. As shown in Fig. 2C, the oil-water distribution coefficients of the four iridium complexes were all above 0.5, falling within the ideal lipophilicity range. The Log *P* values of Ir1-Ir4 were 0.89, 1.02, 0.91, and 0.93, respectively, with Ir2 having the highest lipophilicity of 1.02. Previous studies have shown that there is a relationship between the lipophilicity of metal-based complexes and their cytotoxicity, where higher lipophilicity tends to result in stronger cytotoxicity [34,35]. For some ruthenium [36] and platinum [37] complexes, increased lipophilicity can enhance cellular uptake, thereby leading to enhanced cytotoxicity. Among the four complexes synthesized in this study, based on the high cellular uptake and lipophilicity of Ir2, it exhibited the best cellular activity.

Cell organelles are "miniature organs" within the cytoplasm with specific shapes, structures, and functions. Different organelles have specific functions and work together harmoniously to carry out essential physiological processes within the cell. Many antitumor agents can

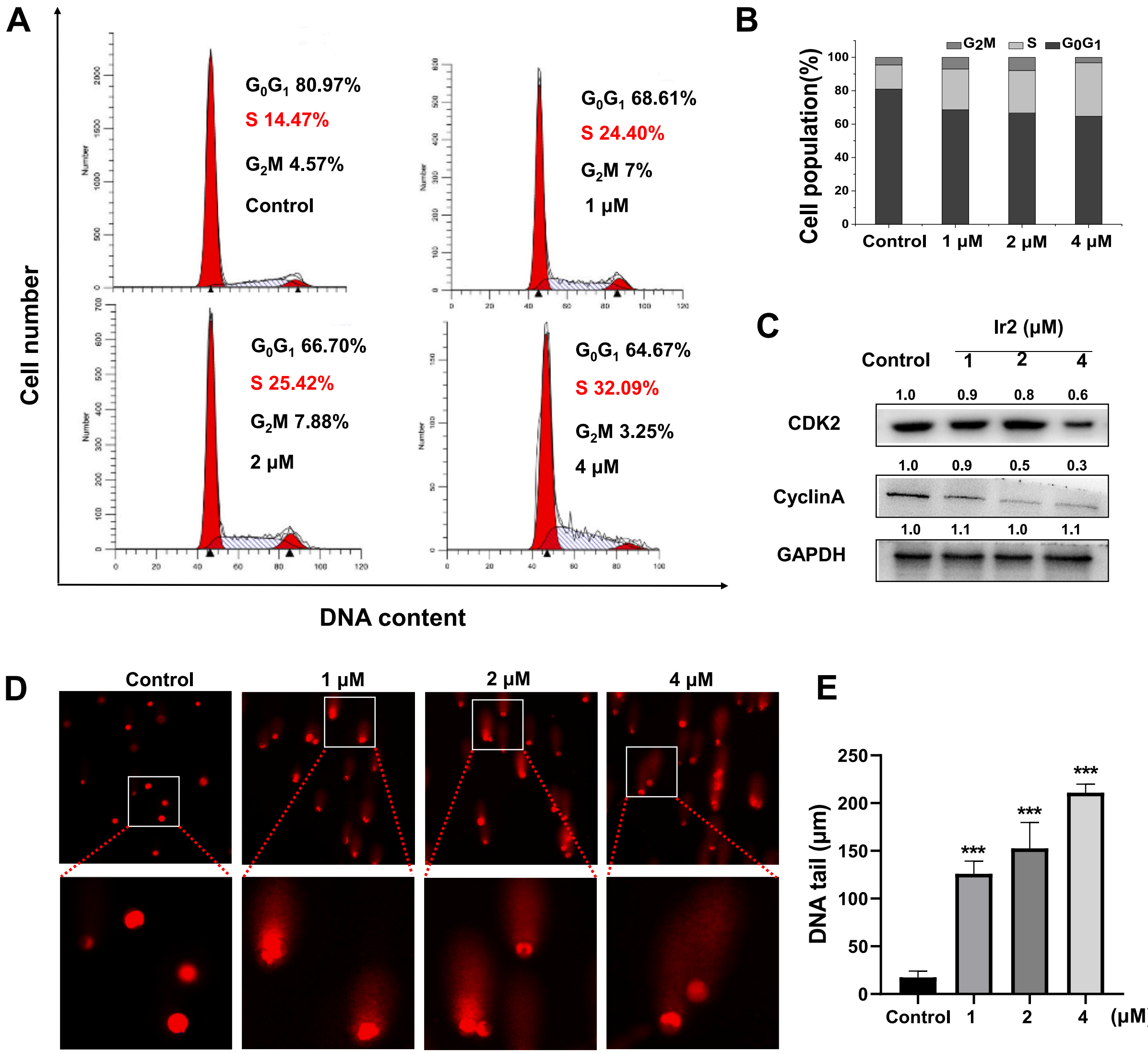

Fig. 4. (A) Distribution of cell cycle of A549 cells incubated with Ir2 (1,2,4 μM) for 12 h, the obtained data from flow cytometry was dealt with FlowJo. (B)The histogram of the cell cycle of A549 cells was treated with Ir2 (1,2,4 μM) for 12 h. (C) Western blotting analysis of CDK2, Cyclin A protein in A549 cells treated with Ir2 (1,2,4 μM) for 12 h. GAPDH was used as an internal control. (D) A549 cells were treated with various concentrations (1,2,4 μM) of Ir2 for 24 h, and DNA fragmentation was examined by comet assay. (E) Quantification of DNA tails in the comet assay. The length of DNA tails in microscopy images was quantified by Image J. The data are presented as mean ± standard deviation (SD) with $^{***}P < 0.001$.

target specific subcellular organelles, accumulate at specific sites, enhance cytotoxic potency, and diminish toxic side effects [38,39]. Investigations have revealed that organometallic compounds can target organelles (e.g., mitochondria, lysosomes, and the nucleus), leading to cellular dysfunction and subsequent organelle damage [40–42]. We used ICP-MS to detect the distribution of iridium complexes in subcellular compartments. As shown in Fig. 2D, after incubating iridium complexes with A549 cells for 24 h, the content of metal iridium in mitochondria increased in a concentration-dependent manner, with Ir2 reaching 344 ± 6.5 ng at a concentration of 4 μM, and the distribution of Ir4 in mitochondria was the second highest, with an iridium content of 290 ± 12.3 ng. Owing to the intrinsic phosphorescence of Ir1-Ir4, their localization within cells can thus be investigated by confocal laser scanning microscopy (CLSM), as shown in Fig. 2E, F. A549 cells were co-incubated with iridium complexes for 3 h, followed by incubation with specific fluorescent probes for mitochondria and lysosomes for 30 min. The Pearson coefficients for the co-localization of Ir1-Ir4 with mitochondria were 0.87, 0.93, 0.81, and 0.89, respectively, consistent with the ICP-MS data in Fig. 2D. Meanwhile, the co-localization coefficients of the complexes with the lysosome-specific dye LysoTracker Deep Red (LTDR, 100 nM) were relatively low, at 0.38, 0.31, 0.34, and 0.27, respectively. These results indicate that Ir1-Ir4 mainly accumulate and localize in mitochondria, potentially inducing cell death through mitochondrial-mediated pathways. According to previous reports, a series of cyclometalated iridium complexes with the same main ligand and only different ancillary ligands should have similar anticancer mechanisms [43]. Since Ir1-Ir4 share the same main ligand (PPA) and exhibit similar activities against the selected tumor cell lines (Table 1), all of them localize to mitochondria, in this work, we selected the most active compound, Ir2, and A549 cells for further investigation into the anticancer mechanisms.

2.4. Mitochondrial dysfunction

Based on the above results, the iridium complexes Ir1-Ir4 were co-localized with mitochondria. Since mitochondria play a crucial role in cellular energy production, a decrease in mitochondrial membrane potential (MMP) can interfere with ATP production in the cell [44]. To verify this, the effect of Ir2 on intracellular ATP levels was measured (Fig. 3A). After incubation of A549 cells with 1, 2, and 4 μM of Ir2 for 12

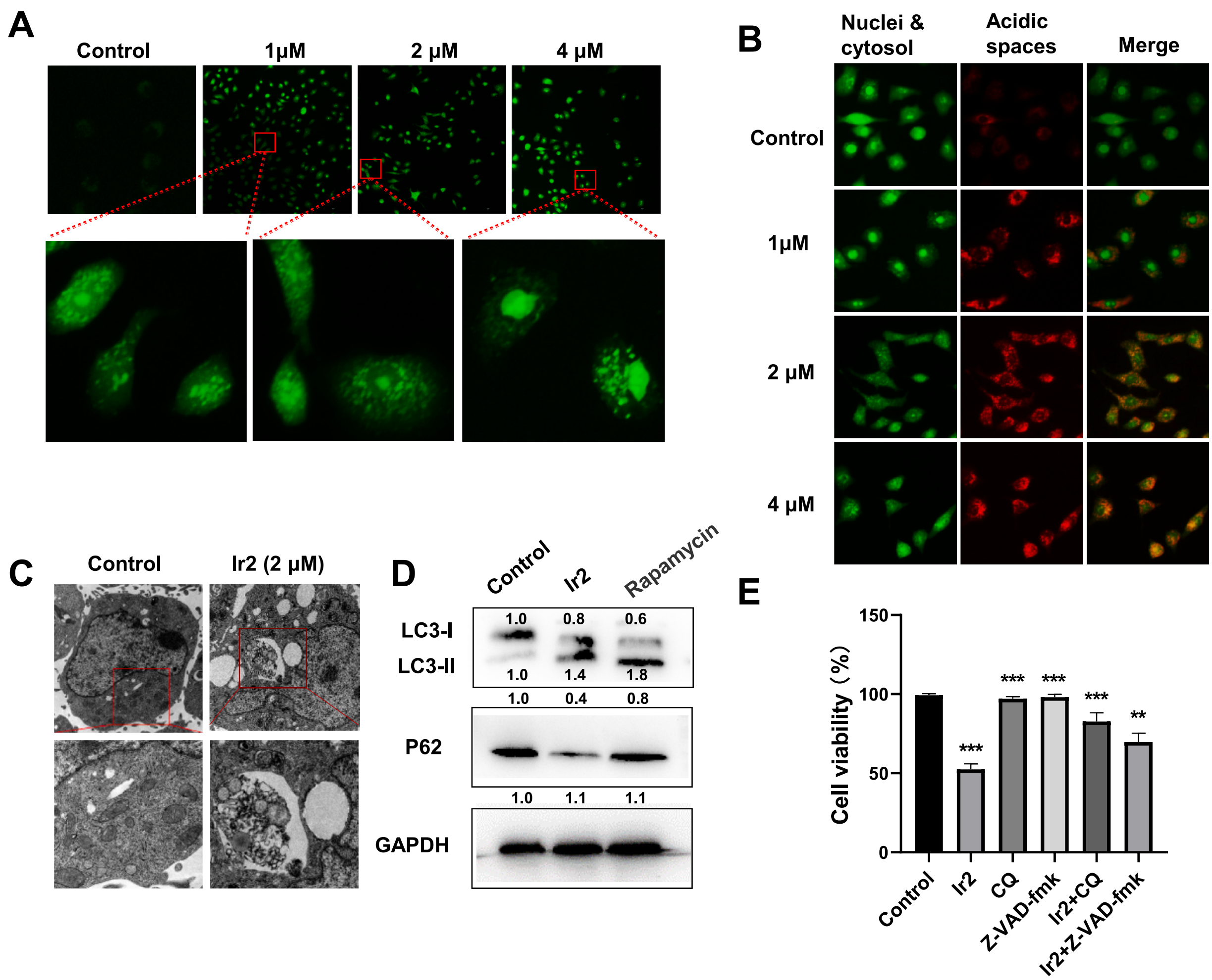

Fig. 5. (A) CLSM images of MDC stained and (B) AO stained A549 cells after treatment with Ir2 (1,2,4 μM) for 12 h. MDC (λ_{ex} = 488 nm, λ_{em} = 518 ± 20 nm), AO (λ_{ex} = 488 nm, λ_{em} = 510 ± 20 nm (green); λ_{em} = 625 ± 20 nm (red). scale bar: 50 μm. (C) TEM images of A549 cells co-labeled with Ir2 (2 μM, 12 h). (D) Western blotting analysis of LC3 protein in A549 cells treated with Ir2 (2 μM) and Rapamycin (1 μM) for 12 h. GAPDH was used as an internal control. (E) The histogram of apoptosis inhibitors *Z*-VAD-fmk (20 μM) and autophagy inhibitors CQ (2.5 μM) on cell viability. The data are presented as mean ± standard deviation (SD) with $^{**}P < 0.01$, $^{***}P < 0.001$. (For interpretation of the references to colour in this figure legend, the reader is referred to the web version of this article.)

h, intracellular ATP levels significantly decreased in a dose- and time-dependent manner. Subsequently, the cell staining was performed using the dye 5,5′,6,6′-tetrachloro-1,1′,3,3′-tetraethylbenzimidazolylcarbocyanine iodide (JC-1), and changes in MMP were detected using fluorescence microscopy. JC-1 is a dual-emission dye that exhibits voltage-dependent accumulation in mitochondria. It can exist as either a green fluorescence monomer in depolarized mitochondria or a red fluorescence aggregate in polarized mitochondria, allowing the evaluation of mitochondrial polarization status through the red/green fluorescence ratio [45]. As shown in Fig. 3B, A549 cells were treated with varying concentrations of Ir2 for 12 h. Compared to the control group, an increase in Ir2 concentration resulted in observable changes from red to green fluorescence, indicating that Ir2 could induce a decrease in MMP.

The mitochondrial respiratory chain is a primary site for the generation of reactive oxygen species (ROS) in organisms [46]. There are reports indicating that the increase of ROS is related to the change of MMP [47]. To investigate the impact of Ir2 on intracellular ROS levels, cell staining with 2′,7′-dichlorodihydrofluorescein diacetate (DCFH-DA) was performed. DCFH-DA is non-fluorescent but can transform into fluorescent DCF when exposed to intracellular ROS. As shown in Fig. 3C, compared to the control group, Ir2 promoted a concentration-dependent increase in the green fluorescence signal of DCF, indicating elevated intracellular ROS levels. Mitochondrial dysfunction can lead to the release of cytochrome *c* from mitochondria, which in turn induces cell apoptosis. Western blot analysis revealed an increase in cytochrome *c* level in the cytoplasm and a decrease in mitochondria (Fig. 3D). This further confirms that the Ir2 complex causes mitochondrial functional damage.

2.5. Induction of cell cycle arrest by Ir2 in A549 cells

One of the characteristics of tumors is the rapid and excessive growth of malignant cells, primarily caused by dysregulation of cell cycle regulation [48,49]. Interfering with cell cycle distribution is regard as one of the most common mechanisms of anti-cancer candidate compounds [50]. Studies have shown that metal-based complexes can inhibit cell division by inducing cell cycle arrest, leading to the suppression of tumor cell proliferation [51]. To investigate the effect of Ir2 on the cell cycle of A549 cells, flow cytometry analysis was performed. As shown in Fig. 4A and B, compared to the control, the percentage of cells in the S phase increased by 7.69% when the concentration of Ir2 was increased from 1 × IC_{50} to 4.0 × IC_{50}. This indicates that Ir2 disrupts the cell cycle, arresting cells in the S phase. It is well known that the progression of the cell cycle is regulated by the formation of a series of specific cyclin-dependent kinases (CDKs) - cyclin complexes. To explore the mechanism by which Ir2 induces cell cycle arrest, we used western blotting to analyze the effect of Ir2 on the expression of CDK2 and Cyclin

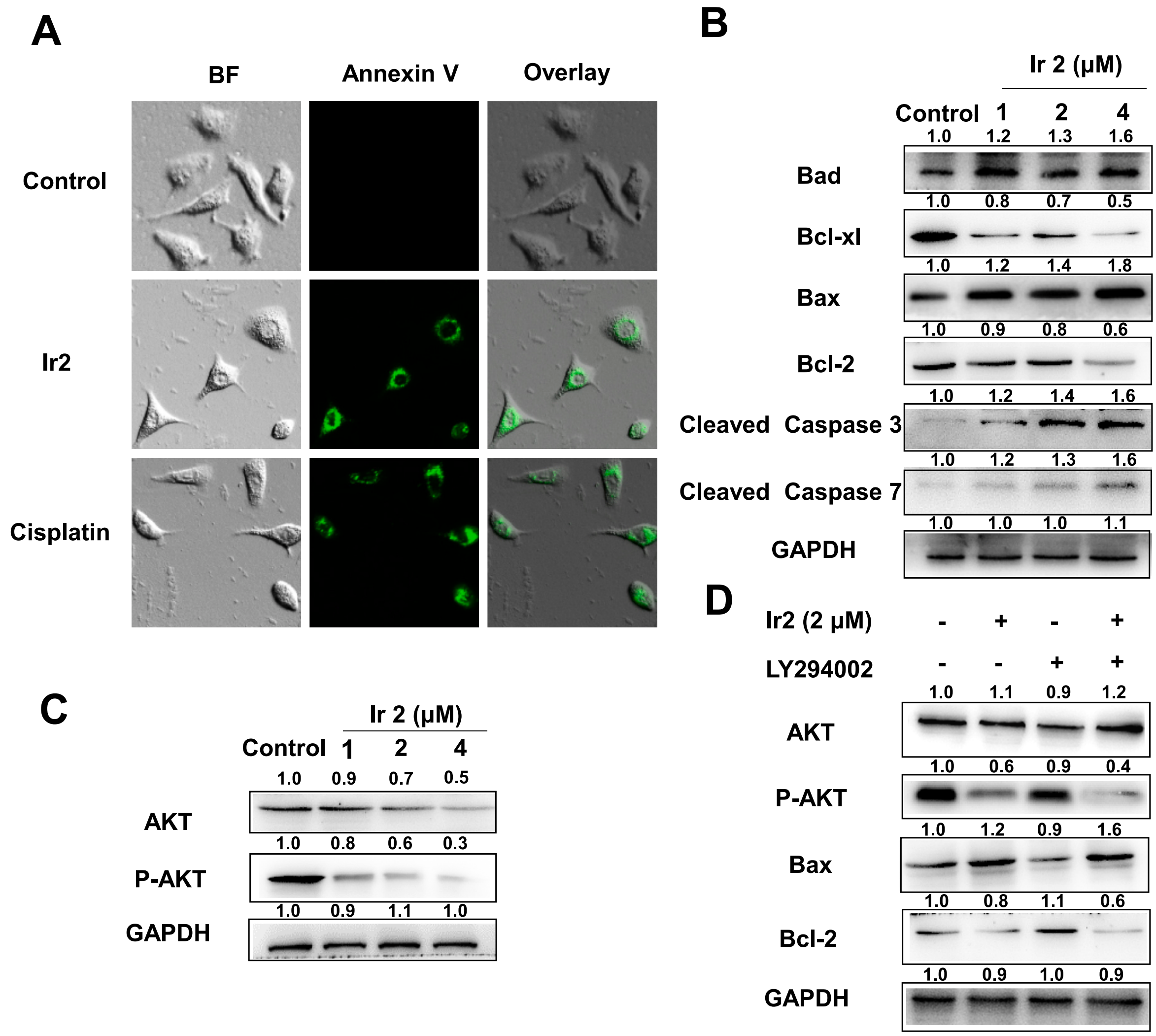

Fig. 6. (A) CLSM images of Annexin V stained A549 cells after treatment with Ir2 (2 μM) and cisplatin (25 μM) for 24 h. (Annexin V: $\lambda_{ex} = 488$ nm; $\lambda_{em} = 525 \pm 25$ nm). scale bar: 50 μm. (B) Western blotting analysis of apoptosis-related protein in A549 cells treated with Ir2 (1,2,4 μM) for 24 h. (C) Western blotting analysis of AKT and P-AKT protein in A549 cells treated with Ir2 (2 μM) and 3-MA for 24 h. (D) Western blotting analysis of apoptosis-related protein in A549 cells treated with LY294002 and Ir2 (2 μM) for 12 h. GAPDH was used as an internal control.

A regulatory proteins. As shown in Fig. 4C, after treatment with Ir2, the expression of CDK2 and Cyclin A decreased in A549 cells. In summary, Ir2 induces cell cycle arrest in the S phase by inhibiting the expression levels of CDK2 and Cyclin A.

DNA damage can lead to inhibition of its replication, failure to repair damaged DNA may induce cell death. Therefore, DNA damage is considered to be a marker of apoptosis [52,53]. Comet assay provides an image of the changes that have happened in the chromatin organization in a single cell, which is regarded as a more effective and simple way to detect DNA fragmentation or DNA damage in a cell population [54]. Hence, we used comet assay to evaluate whether Ir2 could induce DNA damage. As shown in Fig. 4D, no tail appeared in the control group after electrophoresis, but after A549 cells treated with Ir2 for 24 h, the tail of the comet gradually became longer as the concentration of the complex increased, indicating that severe DNA damage has occurred. The length of comet tails was then quantified by Image J software and shown in Fig. 4E, when the concentration of the complex Ir2 reached 4 μM, the length of the comet's tails was about 200 μm. These results suggested that Ir2 could induce DNA damage of A549 cells in a concentration-dependent manner.

2.6. Induction of autophagy by Ir2 in A549 cells

Autophagy serves as an adaptive reaction triggered during periods of stress to uphold cellular energy balance and eliminate protein aggregates as well as impaired organelles via the autolysosomal degradation route [55]. Autophagy requires a large number of autophagy-related proteins (Atgs) and functional complexes [56]. For example, Atg genes regulate the formation of autophagosomes by forming Atg12-Atg5 and LC-II complexes. LC3 family members play a key role in the maturation of autophagosomes, which are the core organelles of autophagy. At the beginning of autophagy, the C-terminal glycine of LC3-I modifies phosphatidyl ethanolamine to form LC3-II, which is rapidly translocated to the neonatal autophagosome in a point-like distribution. Therefore, the expression level of LC3-II is commonly considered as a marker for detecting autophagy [57].To investigate whether Ir2 induces autophagy in A549 cells, we used the specific fluorescent dye Monodansylcadaverine (MDC) to detect the formation of autophagic vacuoles. MDC is an acidotropic dye commonly used as a specific marker for detecting autophagosome formation [58]. As shown in Fig. 5A, no significant green fluorescence puncta were observed in the control group, while bright green fluorescence was visible in A549 cells treated with Ir2 for 12 h, and the MDC fluorescence intensity increased with the

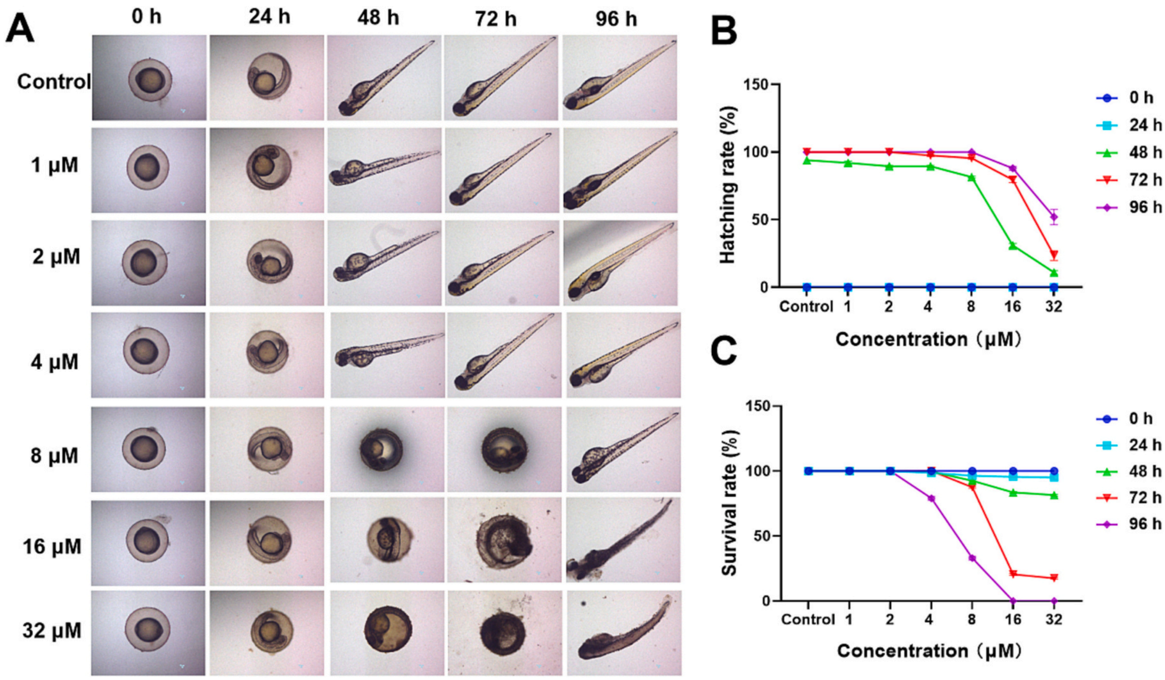

Fig. 7. Toxicity assessment of Ir2 in developing zebrafish embryos. (A) Toxicity of Ir2 to zebrafish embryos at various concentrations within 96 h on a 4 × objective lens in the microscope. (B) Cumulative hatching rate and (C) Survival rate of zebrafish embryos in the presence/absence of Ir2 at various concentrations every 24 h.

increasing concentration of Ir2. These results suggest that Ir2 induces autophagy in A549 cells and promotes the formation of autophagic vacuoles.

Anthracene Orange (AO) is a specific dye that can penetrate intact cell membranes, emitting deep green fluorescence in the cell nucleus and cytoplasm, while displaying red fluorescence in acidic organelles such as acidic vacuolar organelles (AVOAs) and lysosomes [59]. We further used AO staining to confirm whether Ir2 can induce the formation of autophagic vacuoles in A549 cells. In Fig. 5B, the control group showed strong green fluorescence, while the experimental group exhibited significantly enhanced red fluorescence with increasing concentrations of Ir2, indicating that Ir2 can induce the formation of autophagic vacuoles in A549 cells in a concentration-dependent manner. Additionally, we further observed the formation of autophagolysosomes using transmission electron microscopy (TEM). As shown in Fig. 5C, the organelles and nuclear envelope in the control group were intact, with distinct boundaries between organelles, and no apparent fusion was observed. After treatment with Ir2 for 12 h, A549 cells exhibited fusion between mitochondria and lysosomes, indicating the generation of autophagolysosomes.

Furthermore, we examined the expression levels of autophagy-related proteins using a western blotting assay. As shown in Fig. 5D, after 12 h of treatment with Ir2, the conversion of LC3-I to LC3-II occurred, and the expression of LC3-II increased compared to the control group, consistent with the results of autophagy inducer rapamycin. During autophagy, p62 is a commonly used marker protein for measuring autophagic flux [60]. Treatment of A549 cells with Ir2 for 12 h resulted in a decrease in the expression level of p62 protein, indicating the formation of autophagosomes (Fig. 5D). Studies have shown that autophagy is a double-edged sword: on one hand, it can inhibit cell death, while on the other hand, it can accelerate cell death [61].To evaluate the relationship between cell autophagy and cell viability, we used MTT assay to measure the effect of Ir2 on cell viability in the presence of an autophagy inhibitor. As shown in Fig. 5E, co-incubation of the autophagy inhibitor CQ with Ir2 enhanced cell survival. These results suggest that Ir2-induced autophagy in A549 cells is a non-protective mechanism that promotes cell death.

2.7. Induction of apoptosis by Ir2 in A549 cells

Phosphatidylserine (PS) externalization is commonly regarded as a hallmark of early apoptosis [62]. Therefore, Annexin V staining was used to assess the externalization of PS as an indicator of apoptosis induction by the complexes by confocal microscopy. As shown in Fig. 6A, both cisplatin and iridium complexes exhibited significant apoptosis fluorescence signals in cells after 24 h of treatment. Additionally, compared to control cells, most cells treated with cisplatin and Ir2 displayed morphological features characteristic of apoptosis, such as membrane blebbing and cell shrinkage. To further confirm the cell death, we co-treated cells with the apoptosis inhibitor Z-VAD-fmk in combination with Ir2 and measured cell viability using the MTT assay. As shown in Fig. 5E, after 24 h of treatment with Ir2 (2 μM), cell viability in A549 cells was <60% compared to the control group. The apoptosis inhibitor alone did not significantly affect cell viability. However, co-incubation of Z-VAD-fmk with Ir2 noticeably increased cell viability, indicating that the iridium complexes primarily induce cell death through both autophagy and apoptosis.

To further elucidate the mechanism of apoptosis induced by the iridium complexes, we investigated the apoptotic signaling pathways. Protein kinase B (AKT) regulates cell survival and proliferation, playing a crucial role in cell survival and apoptosis by modulating the expression of Bcl-2/Bax proteins [63,64]. Bcl-2/Bax proteins, located upstream of mitochondria, play a critical role in governing the permeability of the mitochondrial membrane, and their overexpression can control the activation of downstream Caspase 3 enzyme, thereby mediating cell death [65]. As shown in Fig. 6B and C, after 24 h of treatment with Ir2, the apoptotic regulatory factor Cleaved caspase 3 and the pro-apoptotic proteins Bad and Bax were upregulated, while AKT, P-AKT, and the anti-apoptotic proteins Bcl-xl and Bcl-2 were downregulated in A549 cells, showing a concentration-dependent change. Based on these findings, we further examined the role of AKT using western blotting assay. As shown in Fig. 6D, pre-treatment with LY294002 (an AKT inhibitor) significantly reduced the expression of P-AKT and Bcl-2 protein. Therefore, we hypothesize that Ir2 primarily induces apoptosis through an AKT-mediated signaling pathway.

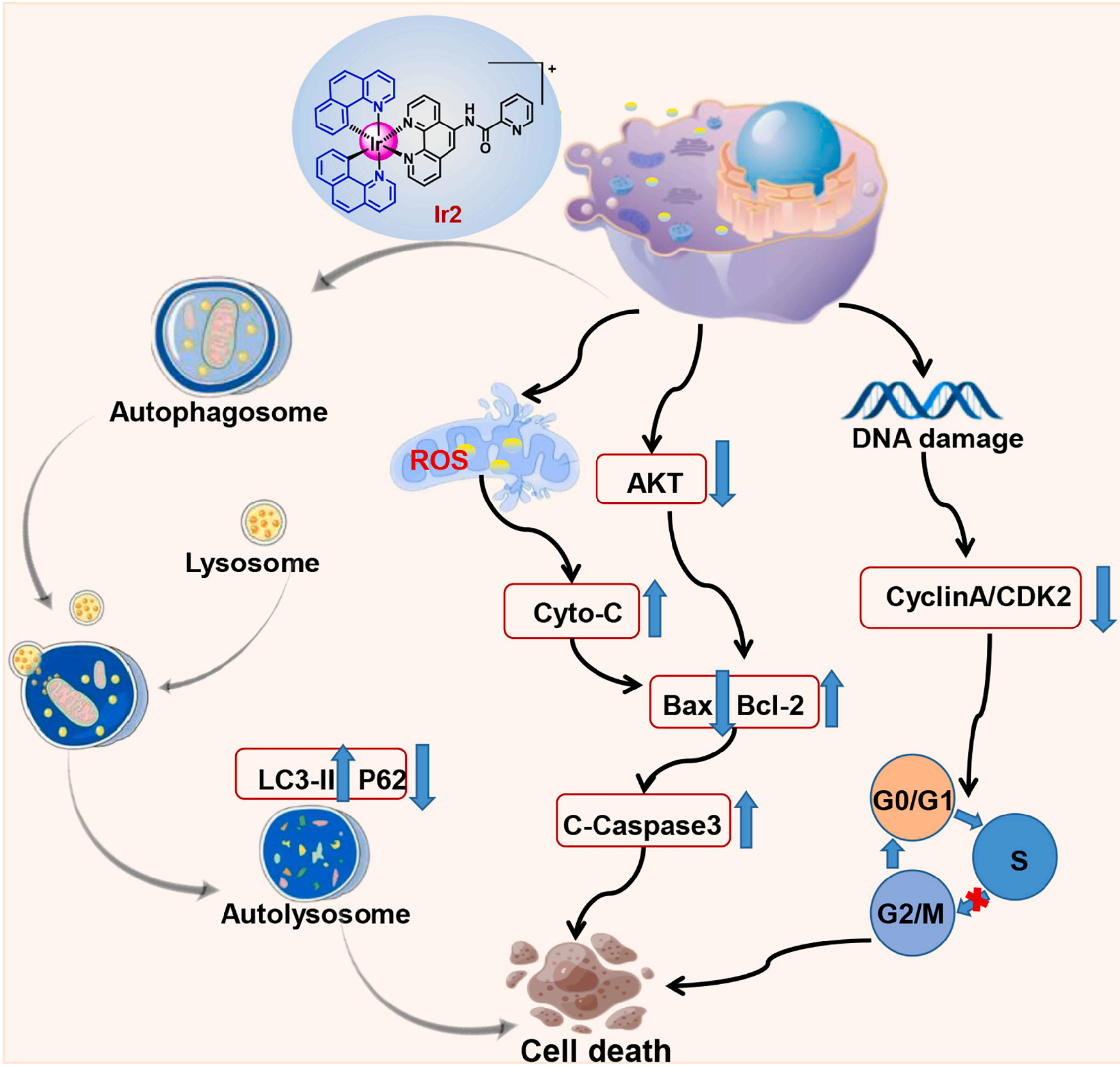

Fig. 8. The main mechanism of apoptosis and autophagy induced by Ir2 in A549 cells.

2.8. *Fish embryo acute toxicity test*

To further investigate the in vivo toxicity of the complexes, we utilized a zebrafish embryo model for in vivo safety assessment. Zebrafish embryos share a high degree of homology with mammals [66], undergo rapid post-fertilization development [67], possess small sizes, and exhibit optical transparency, making them widely used as a biological model for drug discovery and toxicological evaluation. Zebrafish embryos were treated with different concentrations of Ir2, and the cumulative hatching rate and survival rate of embryos were recorded and evaluated every 24 h. The survival and hatching status of embryos were correlated with the concentration of the complexes.

As shown in Fig. 7, the control group exhibited a hatching rate of 93% at 48 h, and nearly all embryos hatched into healthy fish at 72 h without any death or deformities. After adding the Ir2 complex for 96 h, only when the concentration of Ir2 was below 16 μM, the embryo survival rate was higher than 50%, and healthy fish were eventually hatched. However, when the concentration of Ir2 reached 16 μM, the embryo hatching was delayed, and the hatched fish showed morphological deformities with a lower survival rate. At a concentration of 32 μM Ir2, embryos had difficulty hatching, and a few hatched fish exhibited spinal deformities and did not survive. Ir1, Ir3, and Ir4 also showed similar results (Fig. S14 - S16). These findings suggest that the toxicity of Ir2 on zebrafish embryos is relatively low at concentrations below 8 μM, indicating a certain level of in vivo safety. Compared to Ir2, the safe concentrations for zebrafish embryos of Ir1, Ir3, and Ir4 are 16, 32, and 16 μM, respectively.

3. Conclusion

In this study, four metal-based iridium(III) complexes Ir1-Ir4 containing a novel ligand PPA were synthesized and characterized using UV–visible spectroscopy, fluorescence spectroscopy, ^{1}H NMR, elemental analysis, and mass spectrometry. In vitro, cell toxicity experiments demonstrated that complexes Ir1-Ir4 exhibited significant anti-tumor proliferation capabilities, with a certain level of selectivity against normal cells. Cell uptake experiments showed that Ir1-Ir4 could enter cells and located in mitochondria. Among them, Ir2 leads to a decrease in MMP, a decrease in ATP production, and an increase in ROS production. Furthermore, the downregulation of cyclin A expression suggested the inhibition of cell proliferation during the S phase. Mechanism studies revealed that Ir2 induced cell apoptosis and autophagy by activating the AKT-mediated signaling pathway and triggering Bcl-2 family activation (Fig. 8). Autophagy was identified as a non-protective mechanism that promoted cell death. Additionally, in vivo, toxicity experiments indicated that all four complexes exhibited certain safe concentrations in zebrafish embryos, where concentrations below this threshold resulted in embryo hatching and survival rates exceeding 80%

at 96 h. In summary, this series of iridium complexes demonstrated strong anti-cancer activity and could serve as potential candidates for anti-tumor metal-based drugs. This work contributes to a better understanding of the anti-tumor mechanisms of iridium(III) complexes and the design and synthesis of novel metal-based iridium(III) complexes with promising anti-tumor applications.

Credit author statement

Lanmei Chen: Conceptualization, Methodology, Investigation, Formal analysis, Writing - Original Draft

Hong Tang: Conceptualization, Methodology, Investigation, Formal analysis, Writing - Original Draft

Weigang Chen: Methodology, Investigation, Formal analysis, Validation

Jie Wang: Investigation

Shenting Zhang: Investigation

Jie Gao: Investigation

Yu Chen: Investigation

Xufeng Zhu: Resources, Project administration

Zunnan Huang: Resources, Project administration

Jincan Chen: Resources, Writing - review & editing, Project administration

Declaration of Competing Interest

The authors declare that no competing interest exists.

Data availability

Data will be made available on request.

Acknowledgments

This research was funded by the Discipline Construction Project of Guangdong Medical University (4SG23004G), the Science and Technology Program of Zhanjiang (2021A05044, 2021A05242), the Medical Scientific Research Foundation of Guangdong Province of China (A2022026, A2023217), the Science and Technology Program of Guangdong Province (2019B090905011), the Ph.D. Start-up Fund of Guangdong Medical University (4SG23189G) and the University Student Innovation Experiment Program (S202310571050). We thank the Public Service Platform of South China Sea for R&D Marine Biomedicine Resources for support.

Appendix A. Supplementary data

Supplementary data to this article can be found online at https://doi.org/10.1016/j.jinorgbio.2023.112397.

References

[1] F. Bray, J. Ferlay, I. Soerjomataram, R.L. Siegel, L.A. Torre, A. Jemal, CA Cancer J. Clin. 68 (6) (2018) 394–424.
[2] D.M. Hausman, Perspect. Biol. Med. 62 (4) (2019) 778–784.
[3] C. Gridelli, A. Rossi, D.P. Carbone, J. Guarize, N. Karachaliou, T. Mok, F. Petrella, L. Spaggiari, R. Rosell, Nat. Rev. Dis. Primers. 1 (2015) 15009.
[4] S. Walker, Clin. J. Oncol. Nurs. 12 (4) (2008) 587–596.
[5] M. Riihimäki, A. Hemminki, M. Fallah, H. Thomsen, K. Sundquist, J. Sundquist, K. Hemminki, Lung Cancer 86 (1) (2014) 78–84.
[6] V. Pierroz, T. Joshi, A. Leonidova, C. Mari, J. Schur, I. Ott, L. Spiccia, S. Ferrari, G. Gasser, J. Am. Chem. Soc. 134 (50) (2012) 20376–20387.
[7] L. Wang, R. Guan, L. Xie, X. Liao, K. Xiong, T.W. Rees, Y. Chen, L. Ji, H. Chao, Angew. Chem. Int. Ed. Engl. 60 (9) (2021) 4657–4665.
[8] Z.Y. Pan, C.P. Tan, L.S. Rao, H. Zhang, Y. Zheng, L. Hao, L.N. Ji, Z.W. Mao, Angew. Chem. Int. Ed. Engl. 59 (42) (2020) 18755–18762.
[9] J. Liu, H. Lai, Z. Xiong, B. Chen, T. Chen, Chem. Commun. (Camb.) 55 (67) (2019) 9904–9914.
[10] A. Erxleben, Curr. Med. Chem. 26 (4) (2019) 694–728.
[11] R.N. Rao, R.L. Panchangam, V. Manickam, M.M. Balamurali, K. Chanda, ChemPlusChem 85 (8) (2020) 1800–1812.
[12] J. Yellol, S.A. Perez, A. Buceta, G. Yellol, A. Donaire, P. Szumlas, P.J. Bednarski, G. Makhloufi, C. Janiak, A. Espinosa, J. Ruiz, J. Med. Chem. 58 (18) (2015) 7310–7327.
[13] Y. Geldmacher, I. Kitanovic, H. Alborzinia, K. Bergerhoff, R. Rubbiani, P. Wefelmeier, A. Prokop, R. Gust, I. Ott, S. Wolfl, W.S. Sheldrick, ChemMedChem 6 (3) (2011) 429–439.
[14] K. Xiong, Y. Chen, C. Ouyang, R.-L. Guan, L.-N. Ji, H. Chao, Biochimie 125 (2016) 186–194.
[15] A.B. Tamayo, B.D. Alleyne, P.I. Djurovich, S. Lamansky, I. Tsyba, N.N. Ho, R. Bau, M.E. Thompson, J. Am. Chem. Soc. 125 (24) (2003) 7377–7387.
[16] F. Monti, F. Kessler, M. Delgado, J. Frey, F. Bazzanini, G. Accorsi, N. Armaroli, H. J. Bolink, E. Ortí, R. Scopelliti, M.K. Nazeeruddin, E. Baranoff, Inorg. Chem. 52 (18) (2013) 10292–10305.
[17] J.-J. Cao, C.-P. Tan, M.-H. Chen, N. Wu, D.-Y. Yao, X.-G. Liu, L.-N. Ji, Z.-W. Mao, Chem. Sci. 8 (1) (2017) 631–640.
[18] R. Guan, Y. Chen, L. Zeng, T.W. Rees, C. Jin, J. Huang, Z.S. Chen, L. Ji, H. Chao, Chem. Sci. 9 (23) (2018) 5183–5190.
[19] W. Chen, X. Cai, Q. Sun, X. Guo, C. Liang, H. Tang, H. Huang, H. Luo, L. Chen, J. Chen, Eur. J. Med. Chem. 236 (2022), 114335.
[20] J. Chen, Y. Zhang, G. Li, F. Peng, X. Jie, J. She, G. Dongye, Z. Zou, S. Rong, L. Chen, J. Biol. Inorg. Chem. 23 (2) (2018) 261–275.
[21] J. Chen, X. Guo, D. Li, H. Tang, J. Gao, W. Yu, X. Zhu, Z. Sun, Z. Huang, L. Chen, Metallomics 15 (2023) 6.
[22] M. Scheibye-Knudsen, E.F. Fang, D.L. Croteau, D.M. Wilson 3rd, V.A. Bohr, Trends Cell Biol. 25 (3) (2015) 158–170.
[23] S.J. Annesley, P.R. Fisher, Cells 8 (2019) 7.
[24] A.H. Mehler, J. Biol. Chem. 218 (1) (1956) 241–254.
[25] R. Ruffmann, R. Schlick, M.A. Chirigos, W. Budzynsky, L. Varesio, Drugs Exp. Clin. Res. 13 (10) (1987) 607–614.
[26] R.R. Pulimamidi, R. Nomula, R. Pallepogu, H. Shaik, Eur. J. Med. Chem. 79 (2014) 117–127.
[27] H. Hao, X. Liu, X. Ge, Y. Zhao, X. Tian, T. Ren, Y. Wang, C. Zhao, Z. Liu, J. Inorg. Biochem. 192 (2019) 52–61.
[28] H.L. Seng, S.T. Von, K.W. Tan, M.J. Maah, S.W. Ng, R.N. Rahman, I. Caracelli, C. H. Ng, Biometals 23 (1) (2010) 99–118.
[29] M.L. Matlou, F.P. Malan, S. Nkadimeng, L. McGaw, V.J. Tembu, A.E. Manicum, J. Biol. Inorg. Chem. 28 (1) (2023) 29–41.
[30] L. He, C.P. Tan, R.R. Ye, Y.Z. Zhao, Y.H. Liu, Q. Zhao, L.N. Ji, Z.W. Mao, Angew. Chem. Int. Ed. Engl. 53 (45) (2014) 12137–12141.
[31] Y. Zhou, L. Bai, L. Tian, L. Yang, H. Zhang, Y. Zhang, J. Hao, Y. Gu, Y. Liu, J. Inorg. Biochem. 223 (2021), 111550.
[32] G.A. Showell, J.S. Mills, Drug Discov. Today 8 (12) (2003) 551–556.
[33] M. Maschke, H. Alborzinia, M. Lieb, S. Wolfl, N. Metzler-Nolte, ChemMedChem 9 (6) (2014) 1188–1194.
[34] D. Hofer, H.P. Varbanov, M. Hejl, M.A. Jakupec, A. Roller, M.S. Galanski, B. K. Keppler, J. Inorg. Biochem. 174 (2017) 119–129.
[35] V.T. Yilmaz, C. Icsel, O.R. Turgut, M. Aygun, M. Erkisa, M.H. Turkdemir, E. Ulukaya, Eur. J. Med. Chem. 155 (2018) 609–622.
[36] J.Q. Wang, P.Y. Zhang, C. Qian, X.J. Hou, L.N. Ji, H. Chao, J. Biol. Inorg. Chem. 19 (3) (2014) 335–348.
[37] M.R. Reithofer, A.K. Bytzek, S.M. Valiahdi, C.R. Kowol, M. Groessl, C.G. Hartinger, M.A. Jakupec, M.S. Galanski, B.K. Keppler, J. Inorg. Biochem. 105 (1) (2011) 46–51.
[38] J. Liu, Y. Wu, G. Yang, Z. Liu, X. Liu, J. Inorg. Biochem. 239 (2023), 112069.
[39] N.M. Sakhrani, H. Padh, Drug Des. Devel. Ther. 7 (2013) 585–599.
[40] C. Li, Y. Liu, Y. Wu, Y. Sun, F. Li, Biomaterials 34 (4) (2013) 1223–1234.
[41] W.Y. Zhang, Q.Y. Yi, Y.J. Wang, F. Du, M. He, B. Tang, D. Wan, Y.J. Liu, H. L. Huang, Eur. J. Med. Chem. 151 (2018) 568–584.
[42] S.P. Li, C.T. Lau, M.W. Louie, Y.W. Lam, S.H. Cheng, K.K. Lo, Biomaterials 34 (30) (2013) 7519–7532.
[43] J.J. Lu, X.R. Ma, K. Xie, M.R. Chen, B. Huang, R.T. Li, R.R. Ye, Metallomics 14 (2022) 9.
[44] P.J. Burke, Trends Cancer 3 (12) (2017) 857–870.
[45] S.W. Perry, J.P. Norman, J. Barbieri, E.B. Brown, H.A. Gelbard, Biotechniques 50 (2) (2011) 98–115.
[46] Y. Yang, S. Karakhanova, W. Hartwig, J.G. D'Haese, P.P. Philippov, J. Werner, A. V. Bazhin, J. Cell. Physiol. 231 (12) (2016) 2570–2581.
[47] D. Trachootham, J. Alexandre, P. Huang, Nat. Rev. Drug Discov. 8 (7) (2009) 579–591.
[48] U.A. Fahmy, H.M. Aldawsari, S.M. Badr-Eldin, O.A.A. Ahmed, N.A. Alhakamy, H. H. Alsulimani, F. Caraci, G. Caruso, Pharmaceutics 12 (2020) 10.
[49] M.P. Heng, K.S. Sim, K.W. Tan, J. Inorg. Biochem. 208 (2020), 111097.
[50] G. Joshi, P.K. Singh, A. Negi, A. Rana, S. Singh, R. Kumar, Chem. Biol. Interact. 240 (2015) 120–133.
[51] M. Shao, M. Yao, X. Liu, C. Gao, W. Liu, J. Guo, J. Zong, X. Sun, Z. Liu, Inorg. Chem. 60 (22) (2021) 17063–17073.
[52] W.P. Roos, B. Kaina, Trends Mol. Med. 12 (9) (2006) 440–450.
[53] C.C. Zeng, S.H. Lai, J.H. Yao, C. Zhang, H. Yin, W. Li, B.J. Han, Y.J. Liu, Eur. J. Med. Chem. 122 (2016) 118–126.
[54] C. Zhang, S.H. Lai, C.C. Zeng, B. Tang, D. Wan, D.G. Xing, Y.J. Liu, J. Biol. Inorg. Chem. 21 (8) (2016) 1047–1060.
[55] Y. Ohsumi, Cell Res. 24 (1) (2014) 9–23.
[56] B. Tang, D. Wan, Y.J. Wang, Q.Y. Yi, B.H. Guo, Y.J. Liu, Eur. J. Med. Chem. 145 (2018) 302–314.

[57] L. Bai, W.D. Fei, Y.Y. Gu, M. He, F. Du, W.Y. Zhang, L.L. Yang, Y.J. Liu, J. Inorg. Biochem. 205 (2020), 111014.
[58] J. Wang, J. Wang, L. Li, L. Feng, Y.R. Wang, Z. Wang, N.H. Tan, J. Ethnopharmacol. 266 (2021), 113438.
[59] K.Y. Kim, K.I. Park, S.H. Kim, S.N. Yu, S.G. Park, Y.W. Kim, Y.K. Seo, J.Y. Ma, S. C. Ahn, Int. J. Mol. Sci. 18 (2017) 5.
[60] T.T. Xu, H. Li, Z. Dai, G.K. Lau, B.Y. Li, W.L. Zhu, X.Q. Liu, H.F. Liu, W.W. Cai, S. Q. Huang, Q. Wang, S.J. Zhang, Aging (Albany NY) 12 (7) (2020) 6401–6414.
[61] A. Borchers, T. Pieler, Genes (Basel) 1 (3) (2010) 413–426.
[62] R. Kumar, A. Saneja, A.K. Panda, Methods Mol. Biol. 2279 (2021) 213–223.
[63] J. Rodon, R. Dienstmann, V. Serra, J. Tabernero, Nat. Rev. Clin. Oncol. 10 (3) (2013) 143–153.
[64] Y.Y. Hsu, C.M. Liu, H.H. Tsai, Y.J. Jong, I.J. Chen, Y.C. Lo, Toxicology 268 (1–2) (2010) 46–54.
[65] Q.K. Shen, H. Deng, S.B. Wang, Y.S. Tian, Z.S. Quan, Eur. J. Med. Chem. 173 (2019) 15–31.
[66] C. Teijeiro-Valiño, E. Yebra-Pimentel, J. Guerra-Varela, N. Csaba, M.J. Alonso, L. Sánchez, Nanomedicine (Lond.) 12 (17) (2017) 2069–2082.
[67] P. McGrath, C.Q. Li, Drug Discov. Today 13 (9–10) (2008) 394–401.